京都大学防災研究所年報 第 60 号 B 平成 29 年
DPRI Annuals, No. 60 B, 2017

Characterization of Monthly Precipitation over Indochina Region to Evaluate CMIP5 Historical Runs

Rattana CHHIN [(1)], Hoang-Hai BUI [(2)], and Shigeo YODEN [(1)]

(1) Department of Geophysics, Graduate School of Science, Kyoto University
(2) Department of Meteorology, Hanoi University of Science, Vietnam National University, Vietnam

Synopsis

Toward the evaluation of climate simulations, the exploration of local climate contexts is an important step to understand how well the simulation can reproduce that regional climate. In this study, we characterize climatology of precipitation over Indochina Region (ICR) to evaluate CMIP5 historical simulations; such characterization is not much done for this region. After an inter-comparison of four gridded precipitation datasets, we choose APHRODITE for further characterization of the climatology of precipitation for this region. The EOF analysis of APHRODITE dataset for the region shows two dominant precipitation patterns corresponding to the first and second EOFs; the first mode significantly connects with the annual variation of monsoon circulation (monotonic structure), and the second mode more connects with ENSO phenomena (north-south seesaw structure). IOD phenomenon seems to attribute to the first mode rather than the second mode. The time variation of the first two principal components (PCs) from EOF analysis conveys some climate information which is meaningful to evaluate GCMs using those modes. 14 metrics are obtained from this characterization to evaluate CMIP5's GCMs for this region. The initial results based on these metrics suggest that HadGEM2-CC, HadGEM2-ES, MPI-ESM-LR, IPSL-CM5A-LR, and HadGEM2-AO models are the five highest ranking in simulating precipitation over ICR.

Keywords: APHRODITE, CMIP5, GCM, EOF, ENSO, IOD

1. Introduction

Indochina, which includes Myanmar, Thailand, Laos, Cambodia, and Vietnam, is influenced by Asian monsoon system including Indian monsoon, East Asian monsoon, and Western North Pacific monsoon subsystems (Wang et al., 2003; Tsai et al., 2015), and other tropical weather systems (MRC, 2012). The southwest monsoon from mid-May to October, which is the dominant climatic feature in Indochina Region (ICR), generates a distinctly biseasonal pattern of wet and dry periods of more or less equal length (MRC, 2010). Precipitation in ICR is highly and remotely connected with ENSO with negative (positive) anomaly during El Niño (La Niña) phase (Juneng and Tangang, 2005; Kirtphaiboon et al., 2014; Villafuerte and Matsumoto, 2015; Ge et al., 2016; Räsänen et al., 2016).

The evaluation of climate model simulations is important for climate change impact assessment. To achieve this, characterizing the climate features of individual region such as ICR is needed. Each region has its own special climate characteristics which is one of the reasons causing the performance of one climate model to vary spatially (Flato et al., 2013; McSweeney et al., 2015). Moreover, there exist numerous observational or reanalysis datasets to represent weather and climate

variables over the globe, but each dataset also has its own characteristics. Thus, a careful selection of reference dataset (precipitation) is the primary step to evaluate climate model simulations. There are many GCM evaluation studies over the nearby regions, especially India (Raju and Kumar, 2014; Jena et al., 2015; and Raju et al., 2016), but there are few over ICR (Huang et al., 2014). Therefore, more scientific GCM evaluation studies are needed for ICR.

This study evaluates four gridded precipitation datasets (APHRODITE, GPCP, TRMM, CMORPH) against station dataset focusing on ICR; the chosen is used to explore the precipitation characteristics for the IRC. Then, those precipitation characteristics are employed to evaluate CMIP5 historical runs over ICR.

2. Study area

Over Indochina, this study focuses on window area of the longitude 97°E - 110°E and latitude 5°N - 25°N. Map in Fig. 1 shows the topography of the study area. Three important mountain ranges exist at an eastern and western part of the region, and north of Thailand. The northern part of ICR is a foothill of Tibetan plateau.

3. Datasets and Methods

3.1 Observational datasets

Four gridded datasets as listed in Table 1 are among candidates to be compared in this study. The data is obtained in daily timescale except for CMORPH in 3 hourly timescales. Then monthly accumulated precipitation data is constructed from those daily and 3-hourly data.

The station data were obtained from GSOD of National Climate Data Center (NCDC), US, and station observation of Department of Meteorology of Ministry of Water Resource and Meteorology (MOWRAM), Cambodia (Table 2).

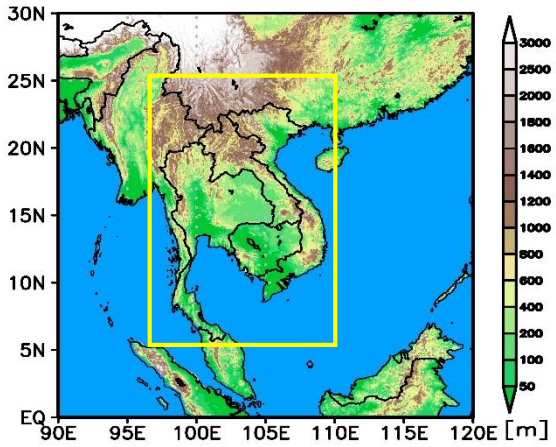

Fig. 1 Topography map of Indochina Region (data from Hastings et al. (1999)). The yellow window is the focus area of this research.

Table 1 Information of gridded precipitation dataset

Dataset	Period	Coverage Area	H_res	Time_res	Institutions	References
APHRODITE (Asian Precipitation - Highly-Resolved Observational Data Integration Towards Evaluation of Water Resources)	1951-2007	Monsoon Asia, 15ºS-55ºN, 60ºE-150ºE, On land only	0.25º x 0.25º	day	RIHN and MRI/JMA	Yatagai et al., 2012
GPCP (Global Precipitation Climatology Project)	1996-2015	Global, Ocean and land	1º x 1º	day	WCRP	Adler et al., 2003
TRMM (Tropical Rainfall Measurement Mission)	1998-2016	Global, 50ºS-50ºN, Ocean and land	0.25º x 0.25º	day	NASA and JAXA	Huffman et al., 2007
CMORPH (NOAA CPC Morphing Technique)	2002-2016	Global, 60ºS-60ºN, Ocean and land	0.25º x 0.25º	3hr	NOAA (CPC)	Joyce et al., 2004

Table 2 Information of station data

Dataset	Period	Number of Stations	Institution	Sources
GSOD (Global Surface Summary of the Day)	1990-Present	396 (Daily)	National Climatic Data Center (NCDC)	Gauge network under World Weather Watch Program of WMO
Station Network of MOWRAM (Ministry of Water Resource and Meteorology of Cambodia)	2000-2013	16 (Daily)	Department of Meteorology of MOWRAM	Station Observation of MOWRAM

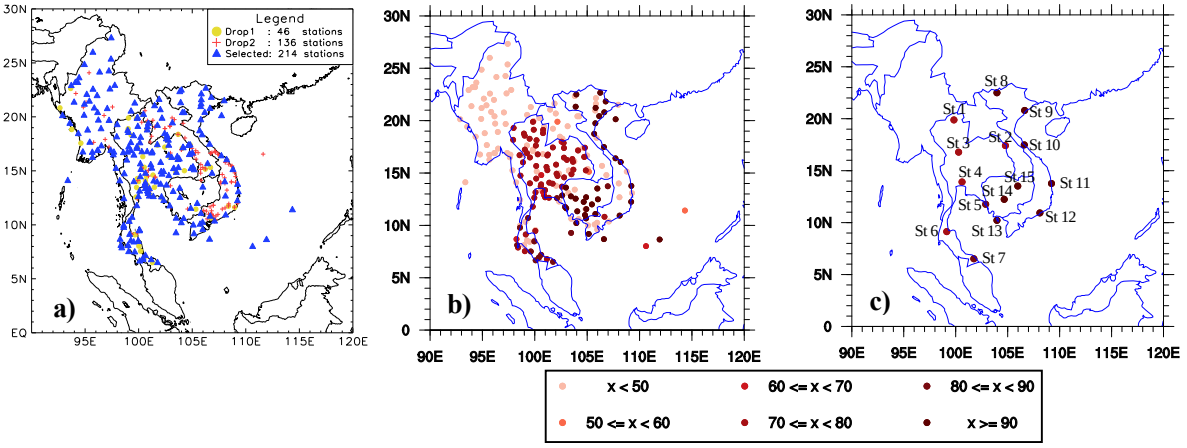

Fig. 2 Map of station locations. a) locations of total 396 stations from GSOD. Filled yellow circles refer to the stations dropped out if the record just started very recently (after 2005), and red plus markers refer to the stations dropped out if the record finished very early (before 2005). b) locations of 230 stations from the combination of selected GSOD stations with stations in Cambodia. The color scales of circle marker show the percentage of non-missing data computed for period 2003-2007. c) the locations of 15 stations selected for inter-comparison with gridded datasets. The numbers closed to markers represent station ID which will be used to identify stations in comparison.

Table 3 List of 43-CMIP5 GCMs to be evaluated in this study

No.	Model Name	Horizontal Resolution	Model Center	Institution
1	ACCESS1-0	1.875° x 1.25°	CSIRO-BOM	CSIRO (Commonwealth Scientific and Industrial Research Organization, Australia), and BOM (Bureau of Meteorology, Australia). (Australia)
2	ACCESS1-3	1.875° x 1.25°		
3	bcc-csm1-1	2.8125° x 64 levels (-87.8638° to 87.8638°)	BCC	Beijing Climate Center, China Meteorological Administration. (China)
4	bcc-csm1-1-m	1.125° x 160 levels (-89.14152° to 89.14152°)		
5	BNU-ESM	2.8125° X 64 levels (-87.8638° to 87.8638°)	GCESS	College of Global Change and Earth System Science, Beijing Normal University (China)
6	CanCM4	2.8125° X 64 levels (-87.8638° to 87.8638°)	CCCma	Canadian Centre for Climate Modelling and Analysis. (Canada)
7	CanESM2	2.8125° X 64 levels (-87.8638° to 87.8638°)		
8	CCSM4	1.25° x 0.94241°	NCAR	National Center for Atmospheric Research. (USA)
9	CESM1-BGC	1.25° x 0.94241°	NSF-DOE-NCAR	National Science Foundation, Department of Energy, National Center for Atmospheric Research. (USA)
10	CESM1-CAM5	1.25° x 0.94241°		
11	CESM1-FASTCHEM	1.25° x 0.94241°		
12	CMCC-CESM	3.75°x 48 levels (-87.15909° to 87.15909°)	CMCC	Centro Euro-Mediterraneo per I Cambiamenti Climatici (Italy)
13	CMCC-CM	0.75° x 240 levels (-89.42708° to 89.42708°)		
14	CMCC-CMS	1.875° x 96 levels (-88.57217° to 88.57217°)		
15	CNRM-CM5	1.40625°x 128 levels (-88.92773° to 88.92773°)	CNRM-CERFACS	Centre National de Recherches Meteorologiques / Centre Europeen de Recherche et Formation Avancees en Calcul Scientifique. (France)
16	CSIRO-Mk3-6-0	1.875° x 96 levels (-88.57217° to 88.57217°)	CSIRO-QCCCE	Commonwealth Scientific and Industrial Research Organisation in collaboration with the Queensland Climate Change Centre of Excellence. (Australia)
17	CSIRO-Mk3L-1-2	5.625° x 56 levels (-87.56134° to 87.56134°)		
18	EC-EARTH	1.125°x 160 levels (-89.14152° to 89.14152°)	EC-EARTH	EC-EARTH consortium (EU)
19	FGOALS-g2	2.8125° x 60 levels (-90° to 90°)	LASG-CESS	LASG, Institute of Atmospheric Physics, Chinese Academy of Sciences; and CESS, Tsinghua University. (China)
20	FGOALS-s2	2.8125° x 180 levels (-88.73009° to 88.73009°)	LASG-IAP	LASG, Institute of Atmospheric Physics, Chinese Academy of Sciences. (China)
21	GFDL-CM3	2.5° x 2°	NOAA GFDL	Geophysical Fluid Dynamics Laboratory (USA)
22	GFDL-ESM2G	2.5° x 90 levels (-89.49438° to 89.49438°)		
23	GFDL-ESM2M	2.5° x 90 levels (-89.49438° to 89.49438°)		
24	GISS-E2-H	2.5° x 2°	NASA GISS	NASA Goddard Institute for Space Studies. (NASA)
25	GISS-E2-R	2.5° x 2°		
26	HadCM3	3.75° x 2.5°	MOHC (additional realizations by INPE)	Met Office Hadley Centre (additional HadGEM2-ES realizations contributed by Instituto Nacional de Pesquisas Espaciais) (UK)
27	HadGEM2-AO	1.875° x 1.25°		
28	HadGEM2-CC	1.875° x 1.25°		
29	HadGEM2-ES	1.875° x 1.25°		
30	inmcm4	2° x 1.5°	INM	Institute for Numerical Mathematics (Russia)
31	IPSL-CM5A-LR	3.75° x 1.89474°	IPSL	Institut Pierre-Simon Laplace (France)
32	IPSL-CM5A-MR	2.5° x 1.26761°		
33	IPSL-CM5B-LR	3.75° x 1.89474°		
34	MIROC-ESM	2.8125° x 64 levels (-87.8638 to 87.8638)	MIROC	Japan Agency for Marine-Earth Science and Technology, Atmosphere and Ocean Research Institute (The University of Tokyo), and National Institute for Environmental Studies. (Japan)
35	MIROC-ESM-CHEM	2.8125° x 64 levels (-87.8638 to 87.8638)		
36	MIROC4h	0.5625° x 320 levels (-89.57009 to 89.57009)		
37	MIROC5	1.40625° x 128 levels (-88.92774 to 88.92774)		
38	MPI-ESM-LR	1.875° x 96 levels (-88.57217 to 88.57217)	MPI-M	Max Planck Institute for Meteorology (MPI-M) (Germany)
39	MPI-ESM-MR	1.875° x 96 levels (-88.57217 to 88.57217)		
40	MPI-ESM-P	1.875° x 96 levels (-88.57217 to 88.57217)		
41	MRI-CGCM3	1.125° x 160 levels (-89.14152 to 89.14152)	MRI	Meteorological Research Institute (Japan)
42	MRI-ESM1	1.125° x 160 levels (-89.14152 to 89.14152)		
43	NorESM1-M	2.5° x 1.89474°	NCC	Norwegian Climate Centre (Norway)

The quality control on GSOD data is needed since there is high rate of un-reported data from some stations. We make two steps of quality control. First, some stations are dropped from a total number of 396 stations over ICR because the record just started very recently (after 2005) referring to drop1 in Fig. 2a, and the record finishes very early (before 2005) referring to drop2 in Fig. 2a. Second, we merge the remaining 214 stations from GSOD with 16 stations from MOWRAM and then compute the percentage of non-missing data of each station as shown in Fig. 2b. Then, 15 stations are subjectively selected from that set of stations based on their high percentages of non-missing data and a uniform spread over ICR (Fig. 2c). These 15-station data will be used to represent precipitation over ICR to evaluate gridded precipitation datasets.

3.2 GCM datasets of CMIP5

In this study, 43 GCM datasets of the Coupled Model Inter-comparison Project Phase 5 (CMIP5) will be evaluated based on the selected dataset over ICR. The model name, horizontal resolution, and institutions of those GCMs are listed in Table 3. The IDs of models are provided based on alphabetical order of model name. The detail information for these GCMs can be found at CMIP5 homepage (http://cmip-pcmdi.llnl.gov/cmip5/).

3.3 Inter-comparison of gridded datasets

Data of fifteen stations are used as references, and the nearest grid to each station's location of the four data sets will be compared. Figure 3 shows Taylor diagrams of the 15-station dataset against the four gridded datasets from 2003 to 2007 based on both daily basis (Fig. 3a), and monthly basis (Fig. 3b). This period is chosen as the overlapping of the four gridded datasets. APHRODITE data has a good correlation with station data with average around 0.75 comparing to the others only around 0.44. However, the standard deviation of APHRODITE is a bit far from reference comparing to the others. Almost all stations from APHRODITE dataset has a very uniform performance (blue markers are very collective on Taylor diagram space), except for the two stations in Cambodia.

For monthly basis, APHRODITE still has a good correlation with the station (average of 0.92), and interestingly, TRMM also has a comparable correlation (average of 0.905) to APHRODITE (Fig. 3b). However, APHRODITE has a more uniform performance than TRMM (all 15 blue markers are closer to each other than

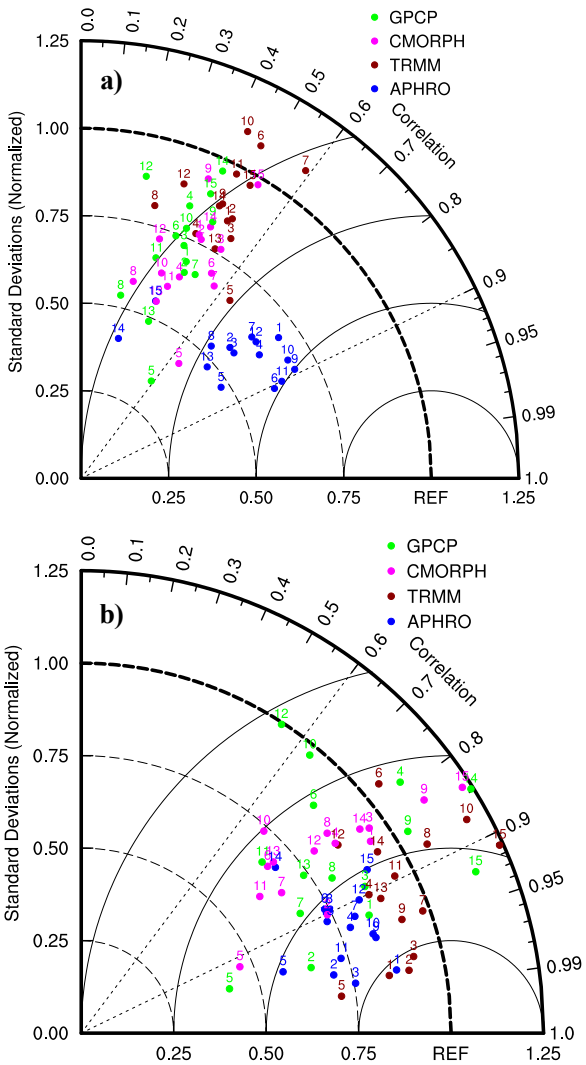

Fig. 3 Taylor diagram of the 15-station over ICR with the four gridded datasets for period 2003-2007 based on daily basis (a) and monthly basis (b).

the red markers). Therefore, APHRODITE is regarded as a proper dataset for the climate study over ICR due to its better representation of precipitation observation and its longer records compared to other gridded datasets.

3.4 Analysis methods

3.4.1 Harmonic Analysis

Harmonic analysis is a technique of representing the fluctuation or periodic variations in time by a sum of basic trigonometric function such as sine and cosine. The general form of the harmonic function is (Wilks, 2011):

$$y_t = \bar{y} + \sum_{k=1}^{n/2} \left\{ C_k \cos\left[\frac{2\pi kt}{n} - \phi_k\right]\right\}, \quad (1)$$

where $\bar{y}$ is time mean of the data, n is number of time points of full data, C_k is amplitude of sinusoidal

function, ϕ_k is phase angle of sinusoidal function, t is a point of time series, k is harmonic number or wave number of cosine function, and $\omega_k = {2\pi kt}/{n}$ is frequency of wave number k.

To estimate the amplitude and phase of that harmonic function for representing the real data, the trigonometric identity is used.

$$\cos(\alpha - \phi) = \cos\alpha\cos\varphi + \sin\alpha\sin\phi, \quad (2)$$

Applying this identity to Eq.1, we get

$$y_t = \bar{y} + \sum_{k=1}^{n/2}\left\{A_k \cos\left[\frac{2\pi kt}{n}\right] + B_k \sin\left[\frac{2\pi kt}{n}\right]\right\}, \quad (3)$$

where A_k, and B_k is estimate from the least-square regression with the form as following:

$$A_k = \frac{2}{n}\sum_{t=1}^{n} y_t \cos\left(\frac{2\pi kt}{n}\right), \quad (4)$$

$$B_k = \frac{2}{n}\sum_{t=1}^{n} y_t \sin\left(\frac{2\pi kt}{n}\right). \quad (5)$$

Then the amplitude and phase of Eq. 1 can be estimated with the following relation:

$$C_k = \sqrt{A_k^2 + B_k^2}, \quad (6)$$

and phase angle is estimated by:

$$\phi_k = \begin{cases} \tan^{-1} {B_k}/{A_k}, & A_k > 0 \\ \tan^{-1} {B_k}/{A_k} \pm \pi, & A_k < 0 \\ {\pi}/{2}, & A_k = 0 \end{cases}. \quad (7)$$

In harmonic model, the displacements of the maximum along the time axis are represented by phase angle charts. This maximum point on that time axis is defined as the maximum occurrence date of the harmonic model (ϕ = 0°, represents 15th December and the other months are represented every 30° and so on) (Kadioglu et al., 1999). This maximum occurrence date can be defined by:

$$t_k = \frac{n}{2\pi}\frac{\phi_k}{k}, \quad (8)$$

where ϕ_k is phase angle for wave number k in radian, and t_k is time point of wave number k (depend on time scale of data).

3.4.2 EOF (Empirical Orthogonal Function) analysis

EOF (Empirical Orthogonal Function) or PCA (Principle Component Analysis) is a multivariate statistical method which reduces a dataset containing a large number of variables into a dataset containing fewer (hopefully many fewer) new variables. These new variables are linear combinations of the original ones, and these linear combinations are chosen to represent the maximum possible fraction of the variability contained in the original data (Wilks, 2011). Suppose $[\mathbf{X}]_{n,p}$ as time space matrix where n is number of observations in the time dimension, and p is number of variables in space dimension.

To operate EOF analysis, the anomaly matrix need to be firstly computed,

$$\mathbf{X'} = \mathbf{X} - \overline{\mathbf{X}}, \quad (9)$$

then the covariance matrix will be determined by,

$$\mathbf{R} = \frac{\mathbf{1}}{\boldsymbol{n-1}}\mathbf{X'^{T}X'}, \quad (10)$$

Where $\mathbf{R}$ is a $p \times p$ symmetric matrix, and $\mathbf{X'^{T}}$ is a $p \times n$ transpose matrix of $\mathbf{X'}$.

In EOF analysis, the covariance matrix will be decomposed by solving simple eigenvalue problem (EVP) which is given as,

$$\mathbf{RE} = \lambda\mathbf{E}, \quad (11)$$

where $\mathbf{E}$ is eigenvector, and λ is eigenvalue.

The principle component time variation signal can be derived by projecting anomaly matrix of the data onto eigenvector by,

$$\mathbf{A} = \mathbf{X'E}, \quad (12)$$

where $\mathbf{A}$ is a $n \times p$ principle component matrix showing the constructed time series from EOF coefficient (eigenvector). The elements in $\mathbf{A}$ are then called principle component (PC).

In this study, we perform statistical analysis on PC time series to observe their relationship with actual precipitation data. Cumulative probability function (CDF) analysis on separated month of inter-annual variation PC time series is made to define an indicator for composite analysis of precipitation. We make a composite average of the precipitation during the years when CDF of PCs for a particular month is larger than 90% or less than 10%. Then we observe the precipitation structure in relation to the extreme groups of the PC time series. Such a way of composite analysis on precipitation is performed for the first two leading PCs.

4. Climatology of precipitation over ICR

4.1 Spatial structure

Figure 4a shows the annual precipitation over the Asian Monsoon region of APHRODITE domain. The high concentrated annual precipitation occurs at the windward side of the mountain range which is oriented against southwest monsoon circulation prevailing over south and Southeast Asia during the rainy season. The average of monthly precipitation over ICR is shown in Fig. 4b. The localized structures of precipitation over this small domain such as along the coastline of Southern Myanmar, along the eastern border of Cambodia, the central part of Laos, and northern Vietnam are observed. Moderate average precipitation is observed at a central part of the region. The standard deviation of monthly precipitation over this region also shows similar localized structures as to those of average precipitation (Fig. 4c). This means that the modulation of precipitation from time-mean (month-to-month variation) also occurs over those localized structures. Interestingly, the magnitude of those local modulation structures is very large, that is to say, equal or even larger than the mean value. This variation may be shaped by the topographic configuration of mountain range against southwest monsoon circulation.

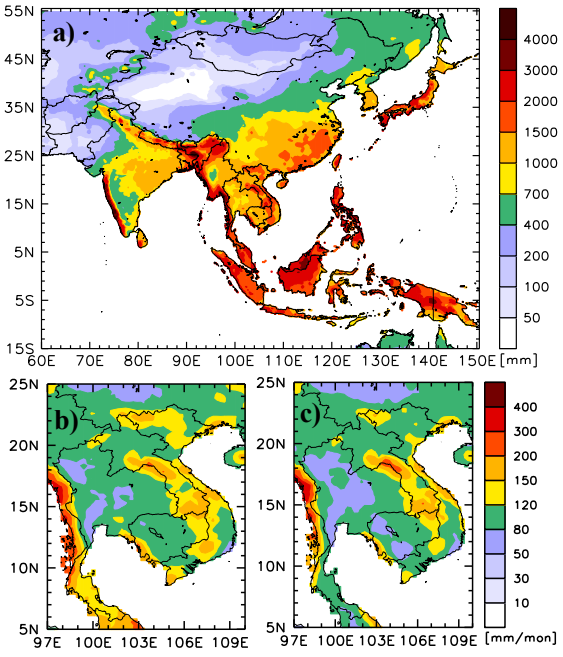

Fig. 4 Precipitation map based on APHRODITE computed for period 1951-2007. a) annual precipitation over whole APHRODITE's domain. b) average of monthly precipitation over ICR. c) standard deviation of monthly precipitation over ICR.

4.2 Harmonic analysis

The harmonic analysis is performed for the climatological seasonal cycle of monthly precipitation to see the month-to-month evolution of precipitation over ICR. The amplitude of harmonic function to represent seasonal cycle of precipitation climatology is shown in Fig. 5a, b, and c corresponding to the first, second, and third harmonic respectively. Similar localized structure to the standard deviation of precipitation appears on the first and the second harmonics. The first harmonic represents the annual variation and the second represents the semi-annual variation of precipitation. Since the fraction of amplitude of second and third harmonic over the first

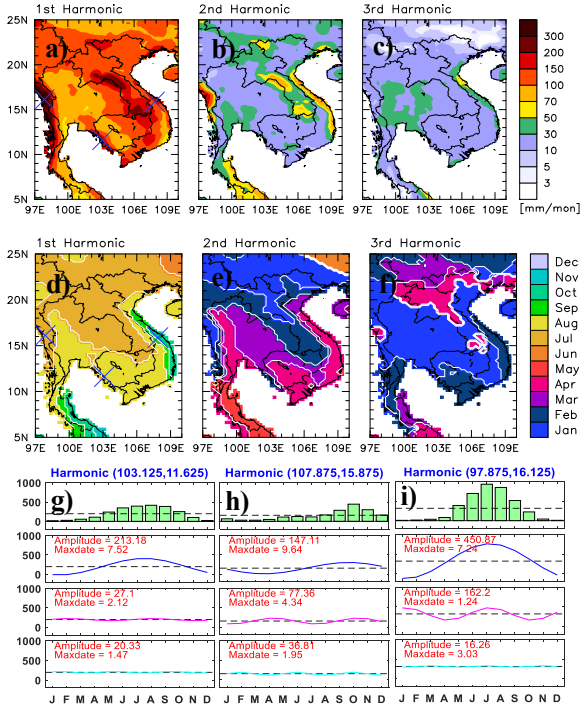

Fig. 5 Harmonic analysis on monthly climatology of precipitation over ICR. a-c) amplitude of harmonic function for wave number one until three. d-f) phase angle of harmonic function converting to maximum occurrence date following Kadioglu et al. (1999). The color scales represent the maximum month of harmonic function. g-i) Examples of harmonic function at three locations (blue cross markers in map of panel a and d) selected based on maximum amplitude on three types of maximum month. Bar plots are actual data, and the three sub-panels below bar plots are the first to third wave of harmonic function to represent actual data. The numbers in brackets at the top of bar plot panel are longitude and latitude of each example location, respectively.

harmonic is below one over this region, the semi-annual variation is not so important for this region (not shown here). However, semi-annual variation of precipitation, maybe to some degree, contains in these two harmonics. Figure 5d, e, and f show the maximum month of harmonic function computed using Eq. (8). The spatial variability of maximum precipitation month occurs around July to October over this region. We show three locations where the amplitude of the first harmonic is maximum, and the same maximum month as an example to illustrate how well the harmonic function represent the actual annual cycle of precipitation (Fig. 5g-i).

5. Space-time variability of precipitation

From the harmonic analysis shown in the previous section, the inter-annual variability of precipitation climatology is not captured. Therefore, we will continue to characterize this information with EOF analysis.

5.1 EOF analysis on monthly precipitation

The results of the EOF analysis on monthly precipitation for period 1951 to 2007 over ICR are illustrated in Fig. 6. The eigenvalue of EOF analysis shows the first mode accounts for 69 %, and the second mode for 10 % of total variance (Fig. 6a). Spatial structure of EOF coefficient (eigenvector) is shown in Fig. 6b (EOF1) and 6c (EOF2). The EOF1 shows a monotonic (positive) pattern over the whole ICR, and localized large positive coefficient occur over the locations similar to the structure of standard deviation of monthly precipitation (Fig. 4c). EOF2 shows a north-south seesaw pattern over this region inferring a non-uniform effect of precipitation variation. The two constructed PC time series from eigenvectors demonstrate a clear seasonal cycle combining with obvious inter-annual variation (Fig. 6d, e). The statistical analysis on these two PCs will show the seasonal and inter-annual variations of precipitation in association with each EOF mode.

5.2 Analyses of PC time series

The composite analysis of precipitation based on CDF of PC1 is illustrated in Fig. 7. Figure 7a shows the climatological mean of PC1 (Black thick solid line), and its inter-annual variations (gray line) fluctuated around this mean value. The positive value of this PC1 score means started from May until October which denotes the rainy season over this region, the same as what noted by

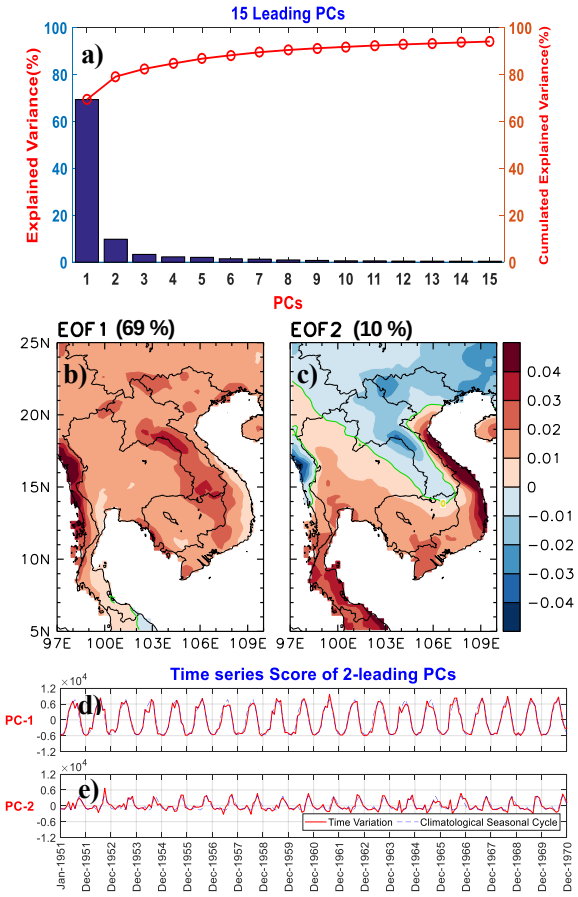

Fig. 6 Results of EOF analysis on monthly precipitation. a) 15 leading principle components (eigenvalue). b-c) the two leading modes of EOF coefficient (eigenvector) over ICR. d-e) Two lead PCs time series (signal) which constructed from eigenvector (zoom in only within 1951-1970). Red solid line is time variation of PCs, and dash blue line is climatological season cycle of PCs.

MRC (2010). The maximum of the mean PC1 occurs in August, and the minimum occurs in January. Zhang et al. (2002) suggested the climatological summer monsoon onset date as on 9th May over this region. The starting month of the above normal of PC1 score here is consistent with onset month of summer monsoon (southwest monsoon). Additionally, Nguyen-Le et al. (2015) who performed EOF analysis on daily rainfall over this region also showed the change of negative to positive value of PC1 during late April.

In this study, the composite of precipitation for the two months is examined in relation to extreme value of PC1. It is observed that the composite precipitation map for CDF larger than 90% shows a wetter condition in the dry season (January) over the whole ICR comparing to that of CDF less than 10% (Fig. 7b, and c). In August, composite

of precipitation map corresponding to CDF larger than 90% also shows a wetter condition over the whole ICR than that of CDF less than 10% (Fig. 7d, and e), where the larger values occur over the same areas as denoted in standard deviation map of monthly precipitation (Fig. 4c).

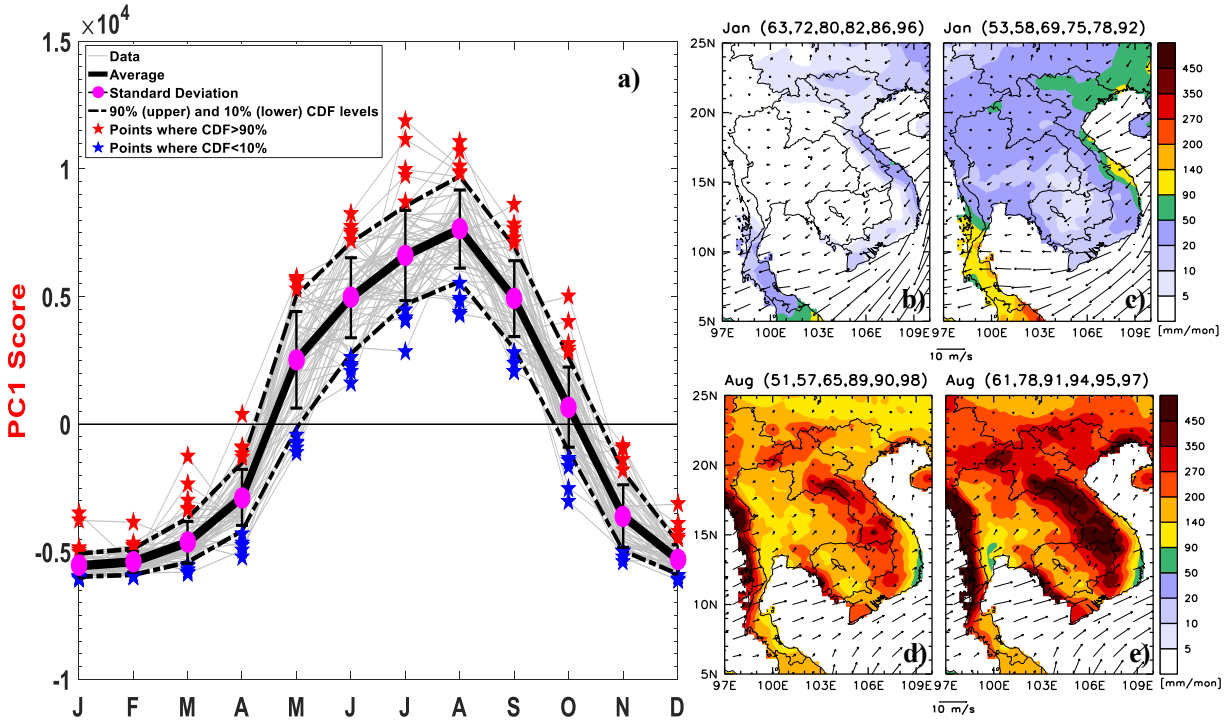

Fig. 7 Composite analysis of precipitation in association with PC1. a) climatological variation of PC1 with inter-annual variation fluctuated around climatological mean (see legend). b) and c) are composite average of precipitation among years (two last digits of year in brackets on the top of each map) corresponding to CDF < 10% and CDF > 90% for January, respectively. d) and e) the same as b) and c), but for August. Note: the wind circulation is based on Japanese 55-year Reanalysis (JRA55) data (1958-2007).

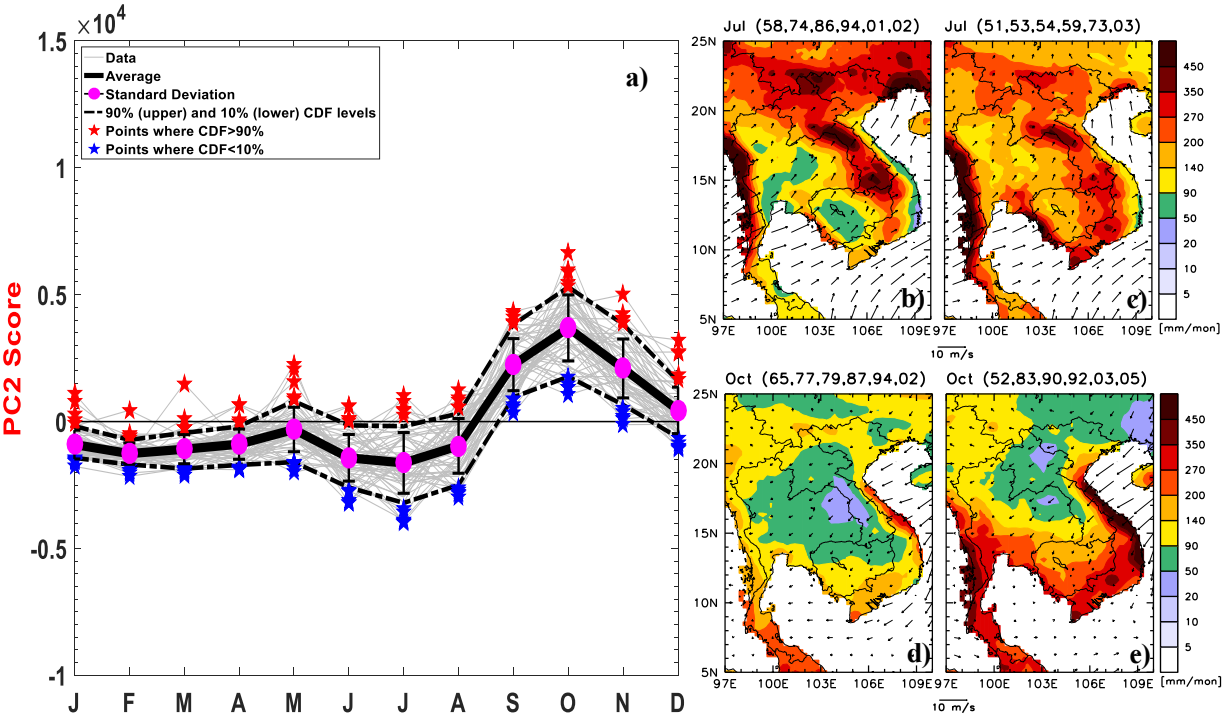

Fig. 8 The same as Fig. 7, but for PC2.

A similar pattern is also observed for other months (not shown here).

The composite analysis of precipitation based on CDF of PC2 is shown in Fig. 8. The month-to-month variation of PC2 is so much different from that of PC1 (Fig. 8a). The maximum value of the climatological mean variation occurs in October, and the minimum occurs in July. The month-to-month evolution of PC2 is consistent with the results from Nguyen-Le at al. (2015), who noted that the annual cycle of PC2 is similar to the seasonal distribution of rainfall in Eastern Indochina Region. This statement is closely related to the work of Wang and LinHo (2002), who also showed a peak rainfall over eastern Indochina Region to occur during September-October. The composite precipitation map of extremely positive and negative of PC2 during the minimum month (July) shows the wetter condition over northern part (north of 20°N) of ICR for CDF less than 10% comparing to that of CDF larger than 90% (Fig. 8b, and c). In October, the wetter condition over the southern part of ICR for CDF larger than 90% comparing that for CDF smaller than 10% clearly appears with the extreme climatological value (Fig. 8d, and e).

From the composite analysis of precipitation based PC1 and PC2 in this study, it is observed that the climatological annual variation of the precipitation over ICR is maintained mostly by the two PCs constructed from EOF1 and EOF2. PC1 shows the fundamental evolution of summer monsoon from onsets to the withdrawal with a peak of precipitation in August. On the other hand, PC2 represent the movement of precipitation area from north to south in the analysis domain. Composite map of precipitation for the extreme years corresponding to CDF less than 10% in July represents more precipitation in the northern part, whereas that of larger than 90% in October represents more precipitation over the southern part.

5.3 Attribution of PC variation

The attribution of the two PC variations is examined with respect to three types of climate phenomena such as monsoon, ENSO (Pacific Ocean oscillation), and IOD (Indian Ocean oscillation). The list of indices to represent those phenomena is given in Table 4, in which the phenomena name, indices' name, derived variables, and references are described. For Indochina monsoon index, four categories of indices are recommended by Tsai et al. (2015), and Southern Myanmar monsoon index and Thailand domain monsoon index are also derived from the four-category indices. To observe the relationship of PCs to those phenomena, correlation analysis of the two-PC signal and time series of the indices is performed. Moreover, the confidence of that correlation is confirmed by student's t test at 95 % confident interval.

The correlation coefficient of PC1 with those indices is illustrated in Fig. 9a. PC1 has a high and significant correlation with most of the monsoon indices, especially, with Indochina monsoon index category 1 and 4 of Tsai et al. (2015). The strong and significant correlation appears when southwest monsoon is active. However, the connection of PC1 with ENSO event is not strong for most of the months, except for April and May. Somehow, the correlation of PC1 with IOD event is moderate; the significant correlation appears during January, February, April, and August.

For PC2, the correlation with monsoon is not as strong as PC1, especially during summer; considerately strong correlation with monsoon still keeps during transition months (dry-wet, and wet-dry month over this region) such as March-May, and September-November (Fig. 9b). In contrast, the correlation of PC2 with ENSO becomes stronger comparing to PC1, especially during October, November, and December. The connection with IOD phenomenon is significant in only two months during October and November.

In summary, the first mode of EOF analysis (PC1) is strongly connected with the monsoon and the second mode (PC2) is connected with ENSO. IOD phenomenon of Indian Ocean connects with PC1 rather than PC2.

6. CMIP5 model evaluation

6.1 Performance metrics

There exist efforts toward improved and more routine evaluations of CMIP models, which require more analysis and researches on performance metrics (Eyring et al., 2016). Along with global effort here, such a kind of efforts should be encouraged for regional scale as well. As part of similar efforts, some metrics are obtained from the method of precipitation characterization to evaluate the 43 GCMs over ICR. Combining with climatological setting analysis of precipitation, 14 metrics are used as indicator for ranking GCMs performance over ICR (Table 5). Among those, four metrics are based on climatological setting analysis, and 10 metrics are based on variability of precipitation applying EOF analysis.

Table 4 List of Indices along with their references for examination of attribution of PCs

Phenomena	Indices	Full Name	Derived Variables	References
Monsoon	**ICMI1**	Indochina Monsoon Index category I	U wind at 850 hPa	Tsai et al., 2015
	ICMI2	Indochina Monsoon Index category II	U wind at 850 hPa	Tsai et al., 2015
	ICMI3	Indochina Monsoon Index category III	U wind at 850 hPa	Tsai et al., 2015
	ICMI4	Indochina Monsoon Index category IV	U wind at 850 hPa	Tsai et al., 2015
	SMMI	Southern Myanmar Monsoon Index	U wind at 850 hPa	Tsai et al., 2015
	TMI	Thailand Domain Monsoon Index	U wind at 850 hPa	Tsai et al., 2015
	IMI	Indian Monsoon Index	U wind at 850 hPa	Wang et al., 2001
	WNPMI	Western North Pacific Monsoon Index	U wind at 850 hPa	Wang and Fan, 1999
ENSO	**SOI**	Southern Oscillation Index	SLP difference	Walker, 1928
	Niño 4	Niño 4	SST anomaly	Rayner et al., 2003
	Niño 3.4	Niño 3.4	SST anomaly	Rayner et al., 2003
	Niño 3	Niño 3	SST anomaly	Rayner et al., 2003
	EMI	El Niño Modoki Index	SST anomaly	Ashok et al., 2007
	PDO	Pacific Decadal Oscillation	Leading PC of monthly SST anomalies in the North Pacific Ocean, poleward of 20N	Mantau et al., 1997
IOD	**DMI**	Dipole Mode Index	SST difference	Saji et al., 1999

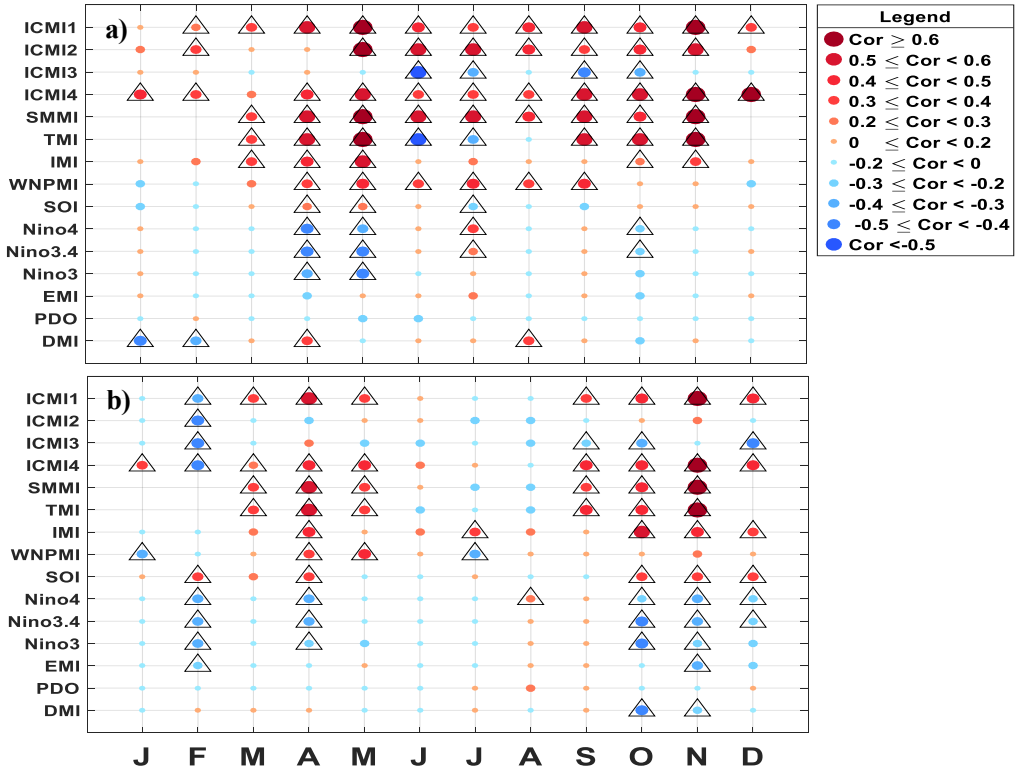

Fig. 9 Correlation coefficient of PCs and some indices (monsoon, ENSO, and IOD). a) for PC1, and b) for PC2. Note: Triangle markers on filled circle markers denote the correlation to be significant based on student's t test for 95% confidence interval.

Table 5 List of 14 performance metrics with their descriptions

Metrics		Description	Climate variables to be evaluated
No	Name		
1	Area Average of Annual Precipitation Bias	Area average of annual precipitation of models minus that of reference	Mean error of annual precipitation
2	Pattern Correlation of Annual Precipitation	Pattern correlation of annual precipitation map of models versus reference.	Spatial distribution of annual precipitation
3	Area Average of STD of Precipitation Bias	Compute standard deviation of monthly precipitation for every grid then average over the study area. Then compute that quantity of models minus reference.	Mean error of modulation of precipitation around mean
4	Pattern Correlation of STD of Precipitation	Pattern correlation of standard deviation (STD) map of models versus reference.	Spatial distribution of modulation of precipitation around mean.
5	Pattern Correlation of FOE1	Pattern correlation EOF1 coefficients (eigenvector) from EOF analysis (models versus reference)	First mode of spatial variability
6	Pattern Correlation of FOE2	Pattern correlation EOF2 coefficients (eigenvector) from EOF analysis (models versus reference)	Second mode of spatial variability
7	RMSE of PC1 Climatology	Compute climatological seasonal cycle of PC1 (a time series constructed from eigenvector). Then compute root mean square error (RMSE) of 12-month evolution (models versus reference).	Error of climatological seasonal cycle of first mode of temporal variability
8	RMSE of PC2 Climatology	Compute climatological seasonal cycle of PC2 (a time series constructed from eigenvector). Then compute root mean square error (RMSE) of 12-month evolution (models versus reference).	Error of climatological seasonal cycle of second mode of temporal variability
9	Correlation of PC1 Time Variation	Correlation of PC1 time series (models versus reference)	Month-to-month variation of first mode of temporal variability
10	Correlation of PC2 Time Variation	Correlation of PC2 time series (models versus reference)	Month-to-month variation of second mode of temporal variability
11	Normalized RMSE of PC1 Time Variation	Normalized RMSE is computed from normalized STD and correlation coefficient using Taylor Diagram space relationship (Taylor, 2001). Compute this quantity of PC1 (models versus reference).	Error of month-to-month variation of first mode of temporal variability
12	Normalized RMSE of PC2 Time Variation	Normalized RMSE is computed from normalized STD and correlation coefficient using Taylor Diagram space relationship (Taylor, 2001). Compute this quantity of PC2 (models versus reference).	Error of month-to-month variation of second mode of temporal variability
13	Correlation of Interannual Variation of PC1	PC1 Time series is decomposed into every month time series (year-to-year time series). Then, compute correlation and p-value of student's t test for that correlation. Then compute the 12-month average of correlation coefficient multiplied with p-value (models versus reference).	Year-to-year variation of first mode of temporal variability
14	Correlation of Interannual Variation of PC2	PC2 Time series is decomposed into every month time series (year-to-year time series). Then, compute correlation and p-value of student's t test for that correlation. Then compute the 12-month average of correlation coefficient multiplied with p-value (models versus reference).	Year-to-year variation of second mode of temporal variability

More importantly, in constructing of PC time series to be meaningful for model comparison, the anomaly field of each model is projected onto EOF (eigenvector) of APHRODITE. It means that PC time series of every model are constructed from Eq. 12 by using only the EOFs that derived from APHRODITE. Since the horizontal resolution of each GCM is different, all GCMs data are interpolated into the same resolution as APHRODITE (0.25° x 0.25°), and then mask out the data over the ocean by keeping the data only inland the same way as APHRODITE. In the ranking matrix, the evaluation is performed during the overlap period between the baseline period of CMIP5 and recorded period of APHRODITE (1951-2005). However, the baseline period of some models is short, for example, from 1961 to 2005. Then, the evaluation of those models is performed only in that period.

6.2 CMIP5 ranking matrix

In the ranking matrix of Table 6, the whiter cell means the model is higher ranking among 43 models and one ensemble average. Metrics number one to four represent the average climatology variable of precipitation. Based on these four metrics, some models have a good ranking (white color) such as CMCC-CMS (model #14), MPI-ESM-MR (#39), MPI-ESM-LR (#38), CMCC-CM (#13), and HadGEM2-CC (#28). However, some models cannot simulate the climatology of this region well such as models bcc-csm1-1 (#3), GISS-E2-R (#25), CSIRO-Mk3-6-0 (#16), MIROC5 (#37), and GISS-E2-H (#24).

Table 6 GCM ranking matrix based on 14 performance metrics

Each metric ranking	1	2	3	4	5	6	7	8	9	10	11	12	13	14	15	16	17	18	19	20	21	22	23	24	25	26	27	28	29	30	31	32	33	34	35	36	37	38	39	40	41	42	43	44
Score-based ranking	1	2	3	4	5	6	7	8	9	10	11	12	13	14	15	16	17	18	19	20	21	22	23	24	25	26	27	28	29	30	31	32	33	34	35	36	37	38	39	40	41	42	43	44

Metrics		**GCMs**																																										
No	**Name**	**1**	**2**	**3**	**4**	**5**	**6**	**7**	**8**	**9**	**10**	**11**	**12**	**13**	**14**	**15**	**16**	**17**	**18**	**19**	**20**	**21**	**22**	**23**	**24**	**25**	**26**	**27**	**28**	**29**	**30**	**31**	**32**	**33**	**34**	**35**	**36**	**37**	**38**	**39**	**40**	**41**	**42**	**43**	**44**
1	Area Average of Annual Precipitation Bias	11	38	41	4	18	3	2	31	30	24	32	37	28	16	29	34	35	14	36	7	5	33	25	42	44	23	15	10	19	40	6	8	9	22	21	43	39	13	1	20	17	12	27	26
2	Pattern Correlation of Annual Precipitation	15	21	41	33	30	32	35	20	18	12	23	24	1	2	31	42	43	9	25	44	16	28	34	38	39	14	5	4	3	36	27	26	40	19	22	17	37	8	6	7	13	11	29	10
3	Area Average of STD of Precipitation Bias	28	42	44	37	11	26	20	24	21	12	25	19	5	2	7	43	41	17	33	4	13	36	35	30	38	9	27	22	29	15	8	6	39	18	16	40	31	1	14	3	34	32	23	10
4	Pattern Correlation of STD of Precipitation	6	13	34	27	23	33	41	12	14	9	16	31	4	5	30	35	25	8	21	39	22	29	37	40	36	20	2	3	1	43	38	32	42	26	28	7	44	11	10	15	19	18	24	17
5	Pattern Correlation of FOE1	4	6	35	29	30	22	23	10	11	9	12	44	16	28	20	33	21	8	32	36	19	27	34	43	37	18	3	2	1	38	26	31	40	41	42	5	39	14	24	13	17	15	25	7
6	Pattern Correlation of FOE2	39	10	44	42	18	23	16	5	4	2	6	22	30	12	33	36	29	1	41	40	20	21	15	38	43	32	34	35	27	28	17	11	37	31	25	7	24	13	8	19	14	26	9	3
7	RMSE of PC1 Climatology	37	44	40	35	5	33	34	3	2	13	6	9	22	15	10	41	42	28	30	11	16	26	21	25	8	27	24	23	31	17	20	18	43	32	29	36	14	12	7	19	39	38	4	1
8	RMSE of PC2 Climatology	5	17	39	38	32	16	8	14	13	10	19	44	40	42	11	34	29	4	43	15	25	30	31	28	21	23	2	7	6	1	9	12	36	24	22	18	3	27	35	26	41	37	33	20
9	Correlation of PC1 Time Variation	39	42	41	43	6	16	29	19	8	31	9	22	25	30	28	26	33	32	40	24	7	4	23	38	34	35	18	13	17	21	20	12	44	27	5	2	10	14	11	15	36	37	3	1
10	Correlation of PC2 Time Variation	12	9	38	40	32	21	17	19	20	11	22	44	43	41	23	27	36	7	37	24	25	26	30	16	15	33	3	10	4	1	5	6	35	18	14	13	2	31	34	28	42	39	29	8
11	Normalized RMSE of PC1 Time Variation	35	43	44	39	3	21	25	18	8	19	9	23	15	20	17	40	41	26	38	14	2	31	32	30	33	28	27	22	29	13	10	7	42	24	12	34	16	5	11	6	36	37	4	1
12	Normalized RMSE of PC2 Time Variation	8	19	43	39	28	11	6	21	20	13	23	44	36	41	17	37	29	9	42	14	24	30	35	31	27	25	2	5	3	1	7	12	34	18	15	16	10	26	33	22	40	38	32	4
13	Correlation of Interannual Variation of PC1	35	40	34	36	33	3	32	20	37	31	27	39	29	22	1	12	26	38	14	24	15	41	9	7	8	21	30	4	5	2	6	23	19	44	11	16	10	25	17	28	13	42	43	18
14	Correlation of Interannual Variation of PC2	27	20	28	17	22	16	42	24	44	23	30	38	26	5	7	21	1	36	3	10	40	29	8	35	34	39	19	6	4	13	11	37	12	25	31	18	14	9	32	2	41	33	43	15
Sum		301	364	546	459	291	276	330	240	250	219	259	440	320	281	264	461	431	237	435	306	249	391	369	441	417	347	211	166	179	269	210	241	472	369	293	272	293	209	243	223	402	415	328	141
Rank		**24**	**30**	**44**	**41**	**21**	**19**	**28**	**10**	**14**	**7**	**15**	**39**	**26**	**20**	**16**	**42**	**37**	**9**	**38**	**25**	**13**	**33**	**31**	**40**	**36**	**29**	**6**	**2**	**3**	**17**	**5**	**11**	**43**	**31**	**22**	**18**	**22**	**4**	**12**	**8**	**34**	**35**	**27**	**1**

The metrics number five and six show the capability of the models to capture spatial variability of precipitation over this region. Based on these two metrics, the models EC-EARTH (#18), ensemble (#44), CESM1-CAM5 (#10), MIROC4h (#36), CCSM4 (#8), and CESM1-BGC (#9) have a better ranking, which means that these models perform well in capturing spatial variability. The worse models in capturing spatial variability of precipitation over this region including models GISS-E2-H (#24), GISS-E2-R (#25), bcc-csm1-1 (#3), IPSL-CM5B-LR (#33) and FGOALS-s2 (#20). Month-to-month time variability of precipitation is represented by the metrics number seven to twelve. The models which can capture this variability include the ensemble (#44), inmcm4 (#30), MIROC5 (#37), IPSL-CM5A-MR (#32), IPSL-CM5A-LR (#31) and CESM1-BGC (#9). The worse models to capture this month-to-month variability include models bcc-csm1-1 (#3), bcc-csm1-1-m (#4), IPSL-CM5B-LR (#33), MRI-CGCM3 (#41), and FGOALS-g2 (#19). The metrics number 13 and 14 represent the inter-annual variability of precipitation. Based on these two metrics, the better ranking models are CNRM-CM5 (#15), HadGEM2-ES (#29), HadGEM2-CC (#28), inmcm4 (#30), and IPSL-CM5A-LR (#31). The worse models to capture the inter-annual variability of precipitation include models NorESM1-M (#43), CESM1-BGC (#9), CMCC-CESM (#12), MRI-ESM1 (#42), and CanESM2 (#7). Therefore, the capability of models to simulate precipitation varies dependent on performance metrics to be evaluated.

The score-based ranking (white-green color scale) is based on the summation of ranking number based on each metric (white-red color scale). This way of scoring can summary the overall performance of models in representing all performance metrics in this study. Based on such a way of ranking, the ensemble average of the 43 GCMs has the highest ranking. The top five models include models HadGEM2-CC (#28), HadGEM2-ES (#29), MPI-ESM-LR (#38), IPSL-CM5A-LR (#31), and HadGEM2-AO (#27). The bottom five worse models include models bcc-csm1-1 (#3), IPSL-CM5B-LR (#33), CSIRO-Mk3-6-0 (#16), bcc-csm1-1-m (#4), and GISS-E2-H (#24) (Table 6).

7. Concluding remarks

We used APHRODITE dataset for characterization of precipitation over Indochina Region (ICR). The pattern of EOF1 accounts for the monotonic seasonal modulation of precipitation over ICR, whereas the pattern of EOF2 characterizes the north-south seesaw pattern. The precipitation variations characterized dominantly by PC1 are influenced from monsoon circulation, whereas those characterized by PC2 are strongly connected with ENSO during wet-dry transition months (October-November). The two modes of EOF analysis of monthly precipitation

over ICR contain climate information which is meaningful to evaluate the GCMs using some related metrics. The advantage of using EOFs is reducing the degree of freedom of precipitation variations over the whole ICR domain into only two modes which are also proved to be connected with precipitation pattern in this region. The ranking matrix based on the 14 metrics in this study suggests the models HadGEM2-CC (#28), HadGEM2-ES (#29), MPI-ESM-LR (#38), IPSL-CM5A-LR (#31), and HadGEM2-AO (#27) are the highest ranking in simulating precipitation over ICR.

Appendix: Model performance based on each metric

A. Annual precipitation

The annual precipitation structure over this region is compared between observation (APHRODITE) and GCMs. The localization of precipitation over this region is shaped by mountain range configuration which is oriented against southwest monsoon circulation. The ability of a model to reproduce this kind of structure is different (Fig. A2). To say something about this, statistical analysis is a good tool for summarizing information of the data. Then, the skill of models to reproduced this annual precipitation structure is evaluated by two metrics namely bias of area average and pattern correlation.

Most of the models overestimate the annual precipitation over this region (Fig. A1a). Ten out of 43 models plus one ensemble average under-estimate the annual precipitation over this region. The top five models that overestimate the annual precipitation including models GISS-E2-H (#24), GISS-E2-R (#25), MIROC4h (#36), inmcm4 (#30), and bcc-csm1-1 (#3). The models that reproduce annual precipitation with small bias from APHRODITE include models MPI-ESM-MR (#39), CanESM2 (#7), CanCM4 (#6), bcc-csm1-1-m (#4), and GFDL-CM3 (#21) (Fig. A1a). The models are ranked based on the absolute bias from the reference (APHRODITE). If the absolute bias of a model approaches zero, that model is ranked higher.

The pattern correlation between annual precipitation map of APHRODITE and that of models is shown in Fig. A1b. The correlation coefficient is plotted against the horizontal resolution of each model's experimental design. The maximum correlation coefficient is approaching 0.6 and the minimum performance of the GCMs in this study even approaches zero (Fig. A1b). In general, the higher horizontal resolution a GCM is, the better performance it is, especially in capturing spatial structure of climate variable. For example, model CMCC-CM (#13), which can reproduce the annual precipitation structure over this region quite well compared to the other models, is experimentally designed with the second highest horizontal resolution among the 43 GCMs in this study. However, the first highest horizontal resolution model (model MIROC4h (#36)) performs lower than the second in capturing annual precipitation structure over this region. Moreover, if we observe the performance of GCMs which come from the same modeling center whose experimental design not so much different, the increase in horizontal resolution makes the performance models in capturing annual precipitation structure over this region better, for instance, Hadley center modeling system (model number 26-29). Anyway, for some modeling center, this assumption is not really true, for instance, MIROC (model number 34-37) (Fig. A1b). Therefore, there should be other factors other than horizontal resolution that make the performance of the models in capturing annual precipitation structure over this region which is not explored in this study.

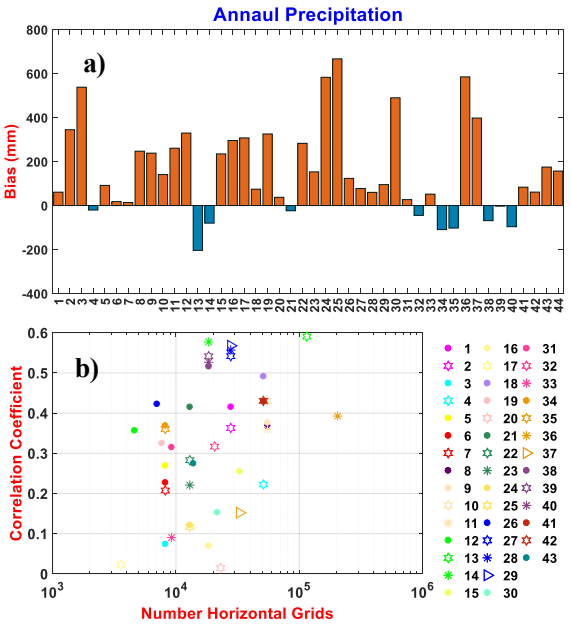

Fig. A1 Model skill in reproducing annual precipitation over ICR. a) bias of area average of annual precipitation map (model minus observation) in millimeter. b) pattern correlation of annual precipitation map between model and observation plotting against horizontal resolution of models. Note: the same color of markers signifies the models which come from the same modeling center, and different symbols of markers signify the different experiment of the same modeling center.

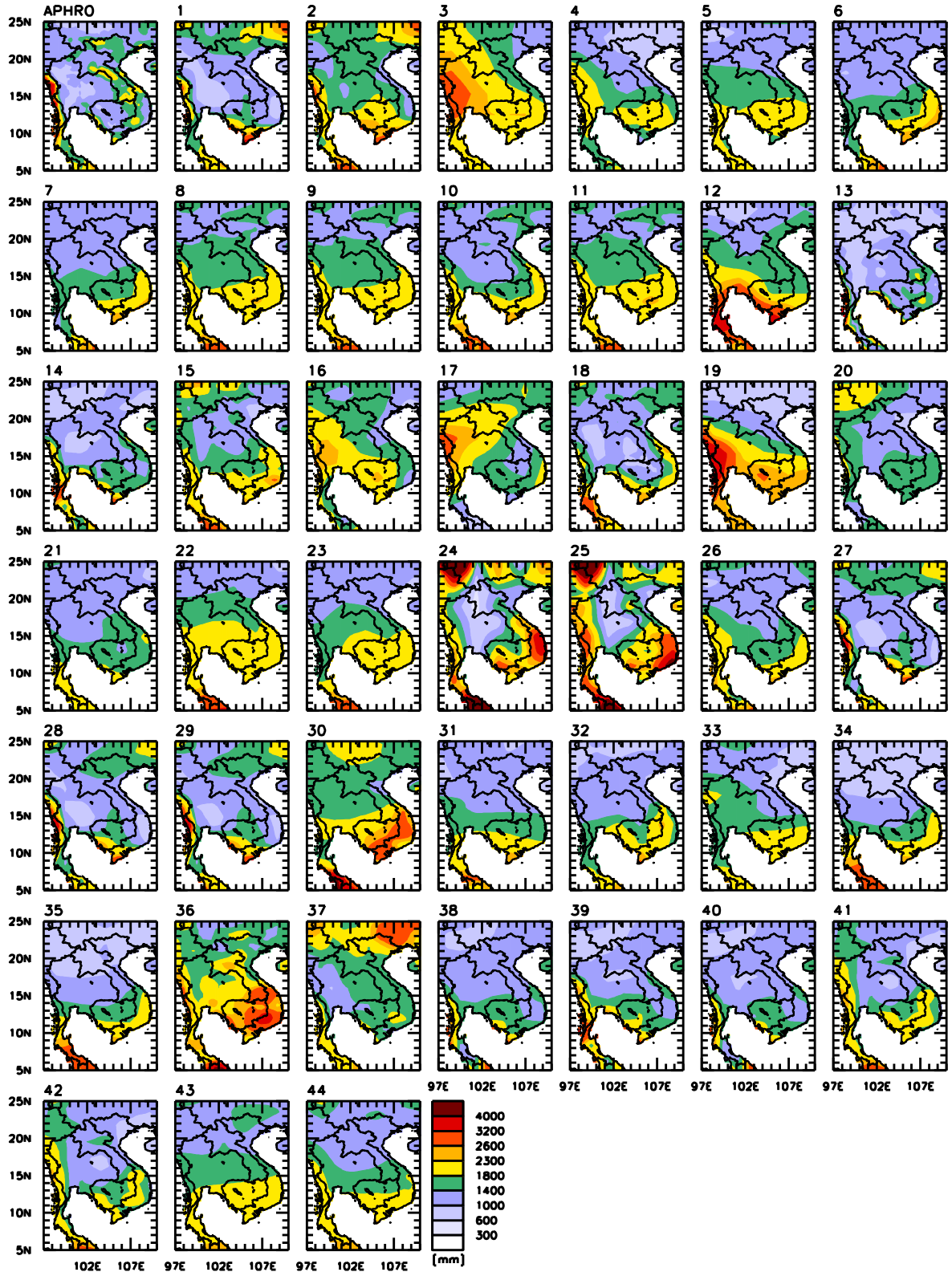

Fig. A2 Annual precipitation map of APHRODITE (the first panel), 43 GCMs (the panel with title from 1 to 43), and ensemble average of 43 GCMs (the last panel with title number 44).

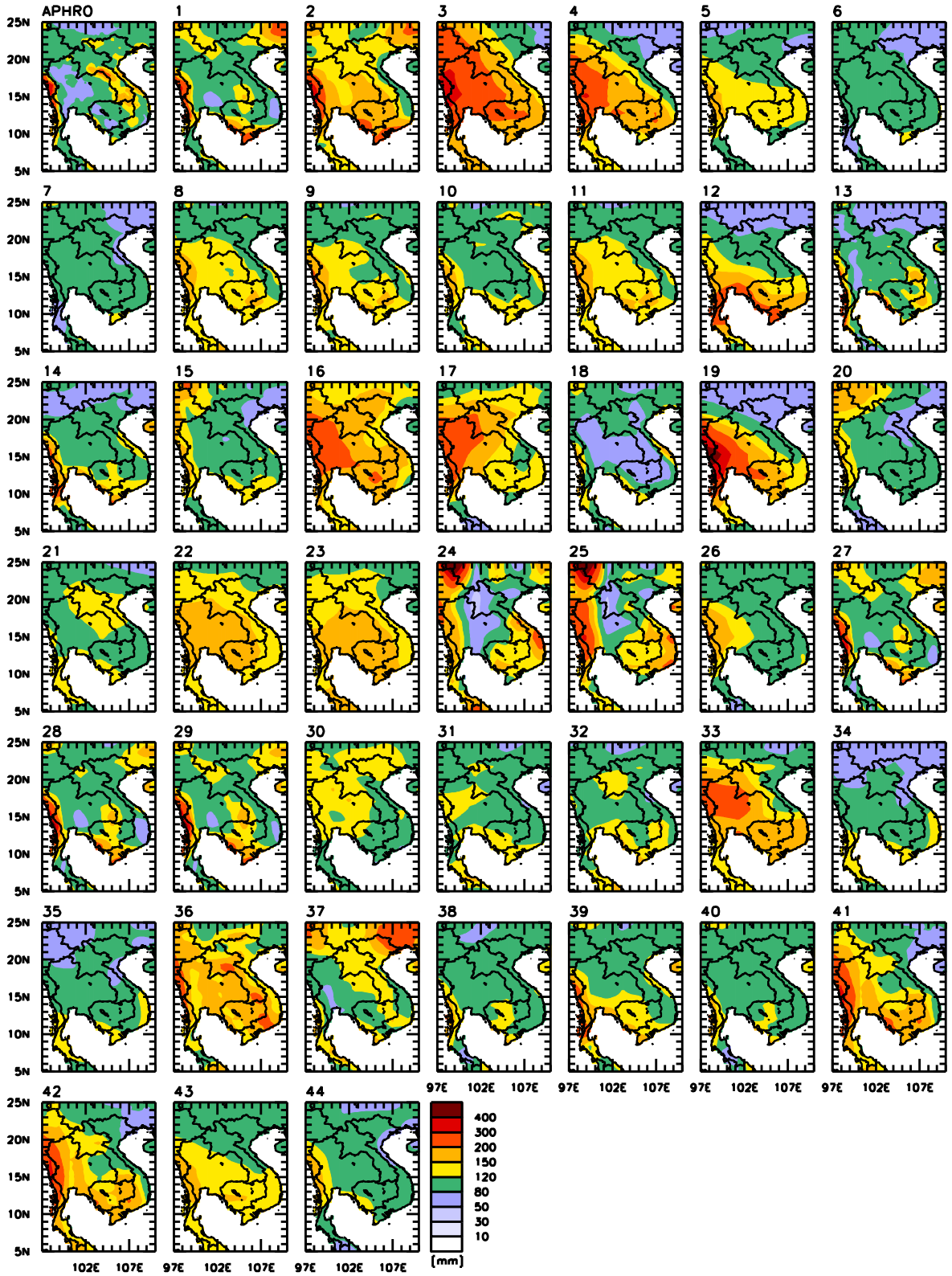

Fig. B1 Standard deviation of precipitation of APHRODITE (the first panel), 43 GCMs (the panel with title from 1 to 43), and ensemble average of 43 GCMs (the last panel with title number 44).

B. Standard deviation of precipitation

The standard deviation (STD) of monthly precipitation is computed for every grid of both reference (APHRODITE) and GCM dataset. The standard deviation map of monthly precipitation is shown in Fig. B1. Some models reproduce monthly precipitation too much deviated, some too much flat, and some similar to the deviation of APHRODITE. The evaluation of this standard deviation map is performed utilizing the similar statistics as annual precipitation map. We observed the bias of area average and pattern correlation between APHRODITE and GCMs of CMIP5.

Among the 43 models and one ensemble average, the maximum bias of deviated precipitation is seen around 75 mm per month from model bcc-csm1-1 (#3). Most of the models are over-deviated from the STD of APHRODITE. Nine over 44 of models are under-deviated from STD of APHRODITE. The top five models that reproduce precipitation with STD similar to that of APHRODITE include models MPI-ESM-LR (#38), CMCC-CMS (#14), MPI-ESM-P (#40), FGOALS-s2 (#20), and CMCC-CM (#13). The bottom five include models bcc-csm1-1 (#3), CSIRO-Mk3-6-0 (#16), ACCESS1-3 (#2), CSIRO-Mk3L-1-2 (#17), and MIROC4h (#36).

Similar to annual precipitation map, the pattern correlation of reference dataset and model datasets is plotted against the horizontal resolution. The maximum correlation coefficient approaches 0.6 which is a moderately high, and the minimum approaches zero. Interestingly, three models of Hadley center modeling system (model HadGEM2-AO (#27), HadGEM2-CC (#28), HadGEM2-ES (#29)) reproduce STD structure of precipitation with a good correlation to the reference, even though their horizontal resolution is smaller than some other models in this study. If compare the model experiments that come from the same modeling center, CMCC of Italy (model number 12-14) shows an increase of correlation when the horizontal resolution increase. However, for MIROC modeling center, they increase horizontal resolution of MIROC5 model (#37), but its performance in capturing STD structure over this region, otherwise, decrease. It seems that along with increasing horizontal resolution, they also change other experimental designs such as physic option in their modeling system. However, the MIROC4h model (#36) of this modeling center shows an increase in correlation when the horizontal resolution increase. Therefore, the performance of models to capture the STD structure over this region depends not only on the horizontal resolution of the model system but also on other experimental designs.

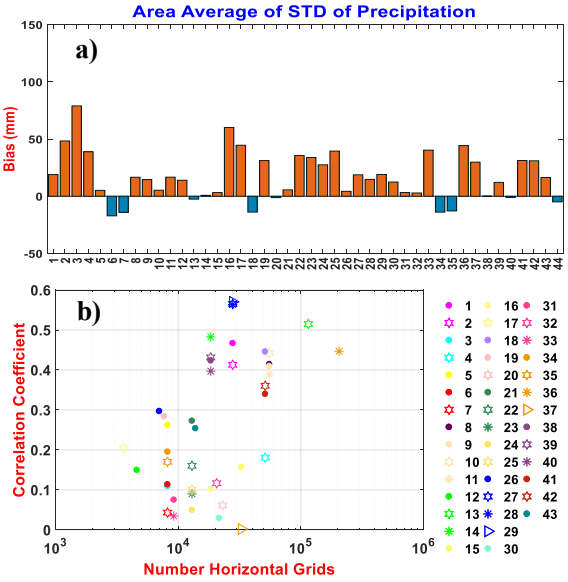

Fig. B2 The same as Fig. A1, but for standard deviation of monthly precipitation.

C. EOF analysis

From EOF analysis on monthly precipitation, two elements are compared such as EOF spatial pattern and PC time series of the first two leading modes. The first mode shows a monotonic pattern which is more connected with monsoon circulation in this region, whereas the second mode shows a north-south seesaw pattern which is more connected with ENSO. By observing how well the models can reproduce these two kinds of structures, the climate variability over this region can be evaluated. From this analysis, 10 metrics are obtained from the statistical analysis of the above-mentioned elements of EOF analysis.

For the EOF1 spatial pattern, all of the models can reproduce the monotonic pattern of this region quite well, but the localized structures of this pattern are lost in most of the models (Fig. C1). For EOF2 spatial pattern, all models can reproduce the seesaw pattern over this region well, but the locations of zero line of this pattern are not so consistent with those of APHRODITE (Fig. C2). This probably highly connects with the horizontal resolution of model experimental design. The pattern correlation between reference and models for the two modes is performed. For EOF1, the correlation coefficient is ranged from 0.09 to 0.7, and EOF2 from 0.55 to 0.9 (not shown here). Most of the models can capture the structure of EOF2 better than EOF1.

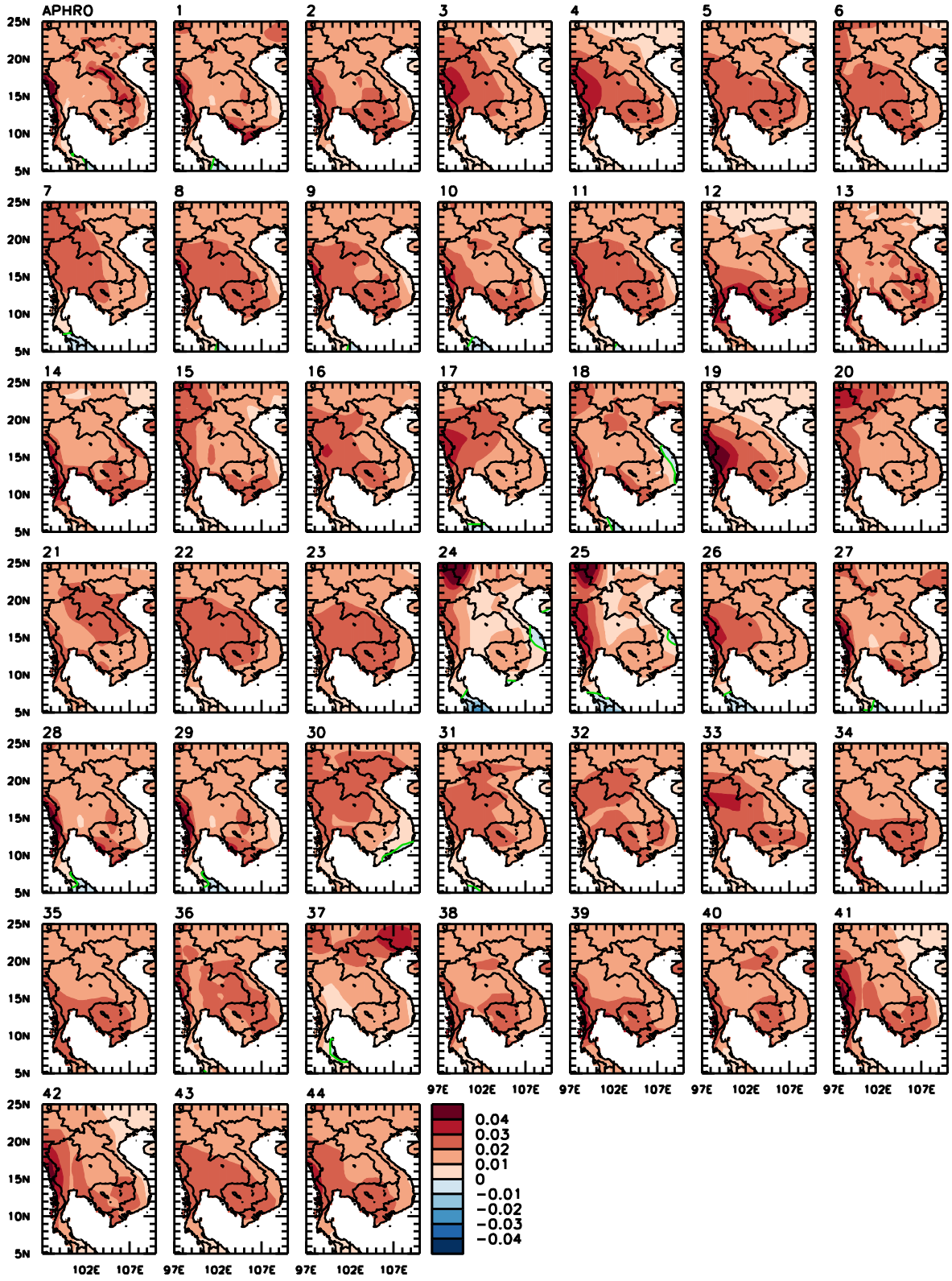

Fig. C1 EOF1 spatial pattern of APHRODITE (the first panel), 43 GCMs (the panel with title from 1 to 43), and ensemble average of 43 GCMs (the last panel with title number 44).

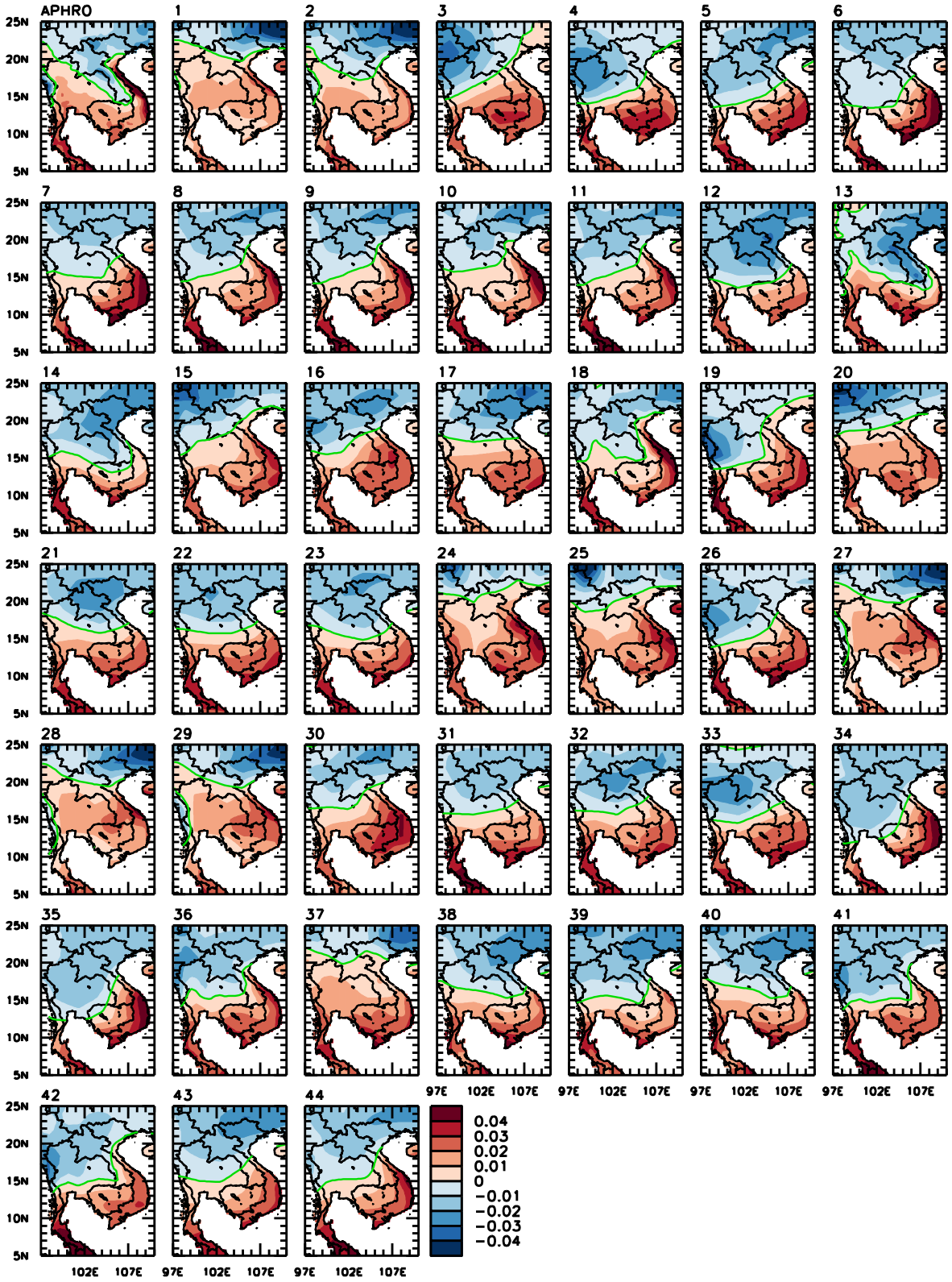

Fig. C2 EOF2 spatial pattern of APHRODITE (the first panel), 43 GCMs (the panel with title from 1 to 43), and ensemble average of 43 GCMs (the last panel with title number 44).

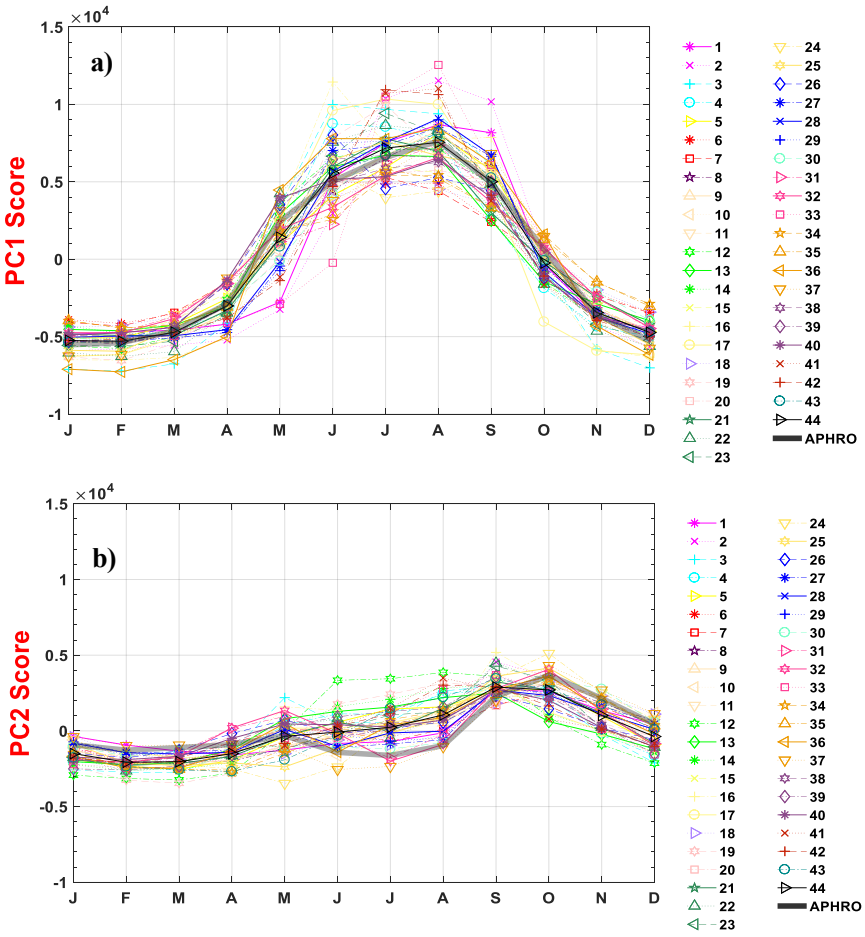

Fig. C3 Annual cycle of PCs time series constructed by projecting the anomaly fields of models onto EOF of the reference dataset (APHRODITE). a) PC1 and b) PC2.

For PC time series, eight metrics are obtained for evaluating GCMs such as based on the annual cycle, full-time series (month-to-month variation time series), and interannual (year-to-year variation time series) of these PC time series. The annual cycle of PC time series is shown in Fig. C3. All of the models can reproduce the unimodal pattern of PC1 very well, but some degree of bias from reference are observed. However, for PC2, some models cannot reproduce the bimodal pattern of the annual cycle of this region well such as CMCC-CESM model (#12). The root mean square error (RMSE) between the reference and the models is computed to evaluate model skill in reproducing this annual cycle. The smaller the RMSE, the higher ranking a model is.

Based on full PC time series, two statistics are computed such as correlation coefficient and normalized root mean square error (NRMSE) using Taylor diagram space relationship (Taylor, 2001). The correlation coefficient of PC1 time series of all models is ranging from 0.82 to 0.96, and the ensemble average has the highest correlation to the reference (not shown here). For PC2 time series, the correlation coefficient is ranging from 0.3 to 0.8, and the inmcm4 model (#30) is the highest followed by MIROC5 model (#37). The higher the correlation, the higher ranking a model is. Based on NRMSE, the value of this statistic for PC1 is ranging from 0.3 to 0.85 with the ensemble average as the lowest error (not shown here). For PC2, the value of this statistic is ranging from 0.7 to 1.82 with the inmcm4 model (#30) as the lowest error. Therefore, all the models make a larger error in reproducing PC2 time series than that of PC1.

Finally, the full PC time series are rearranged into inter-annual time series of every month. Then, the correlation of these inter-annual time series is computed. All of the models make a poor correlation with the reference based on these inter-annual time series; less than 0.3 for PC1 and less than 0.4 for PC2 (not shown here). However, the value that reaches to the above value is quite randomly to one or two months. The value frequently around 0.1 for all the models. Therefore, the model skill to reproduce this inter-annual variation is still limited.

Acknowledgements

This work is supported by JSPS KAKENHI Grant Numbers JP24224011 and JP17H01159, and JSPS Core-to-Core program, B. Asia-Africa Science Platforms.

References

Adler, R.F., Huffman, G.J., Chang, A., Ferraro, R., Xie, P., Janowiak, J., Rudolf, B., Schneider, U., Curtis, S., Bolvin, D., Gruber, A., Susskind, J., and Arkin, P. (2003): The Version 2 Global Precipitation Climatology Project (GPCP) Monthly Precipitation Analysis (1979-Present). *J. Hydrometeor.*, **4**, pp. 1147-1167.

Ashok, K., Behera, S.K., Rao, S.A., Weng, H., and Yamagata, T. (2007): El Niño Modoki and its possible teleconnection. *J. Geophys. Res.*, **112**, p. C11007. DOI:10.1029/2006JC003798

Eyring, V., Gleckler, P.J., Heinze, C., Stouffer, R. J., Taylor, K.E., Balaji, V., Guilyardi, E., Joussaume, S., Kindermann, S., Lawrence, B.N., Meehl, G.A., Righi, M., and Williams, D.N. (2016): Towards improved and more routine Earth system model evaluation in CMIP, *Earth Syst. Dynam.*, **7**, pp. 813-830. DOI: 10.5194/esd-7-813-2016

Ge, F., Zhi, X.F., Babar, Z.A., Tang, W., and Chen, P. (2016): Interannual Variation of Summer Monsoon Precipitation over the Indochina Peninsula in Association with ENSO, *Theor Appl Climatol*, **128-3**, pp. 523–531. DOI: 10.1007/s00704-015-1729-y

Flato, G., Marotzke, J., Abiodun, B., Braconnot, P., Chou, S.C., Collins, W., Cox, P., Driouech, F., Emori, S., Eyring, V., Forest, C., Gleckler, P., Guilyardi, E., Jakob, C., Kattsov, V., Reason, C. and Rummukainen, M. (2013): *Evaluation of Climate Models. In: Climate Change 2013: The Physical Science Basis. Contribution of Working Group I to the Fifth Assessment Report of the Intergovernmental Panel on Climate Change* [Stocker, T.F., D. Qin, G.-K. Plattner, M. Tignor, S.K. Allen, J. Boschung, A. Nauels, Y. Xia, V. Bex and P.M. Midgley (eds.)]. Cambridge University Press, Cambridge, United Kingdom and New York, NY, USA.

Hastings, David, A., and Paula, K. Dunbar (1999): Global Land One-kilometer Base Elevation (GLOBE) Digital Elevation Model, Documentation, Volume 1.0. Key to Geophysical Records Documentation (KGRD) 34. National Oceanic and Atmospheric Administration, National Geophysical Data Center, 325 Broadway, Boulder, Colorado 80303, U.S.A.

Huang, Y., Wang, F., Li, Y., and Cai, T. (2014): Multi-model ensemble simulation and projection in the climate change in the Mekong River Basin. Part I: temperature, *Environ Monit Assess*, **186**, pp. 7513-7523. DOI: 10.1007/s1066-014-3944-x

Huffman, G.J., Adler, R.F., Bolvin, D.T., Gu, G., Nelkin, E.J., Bowman, K.P., Hong, Y., Stocker, E.F., Wolff, D.B. (2007): The TRMM Multi-satellite Precipitation Analysis: Quasi-Global, Multi-Year, Combined-Sensor Precipitation Estimates at Fine Scale. *J. Hydrometeor.*, **8**, pp. 38-55.

Jena, P., Azad, S., and Rajeevan, M.N. (2015): Statistical Selection of the Optimum Models in the CMIP5 Dataset for Climate Change Projection of Indian Monsoon Rainfall, *climate*, **3**, pp. 858-875. DOI: 10.3390/cli3040858

Joyce, R.J., Janowiak, J.E., Arkin, P. A., and Xie, P. (2004): CMORPH: A method that produces global precipitation estimates from passive microwave and infrared data at high spatial and temporal resolution, *J. Hydromet.*, **5**, pp. 487-503.

Juneng, L., and Tangang, F.T. (2005): Evolution of ENSO-related Rainfall Anomalies in Southeast Asia Region and its Relationship with Atmosphere-Ocean Variations in Indo-Pacific Sector, *Climate Dynamics*, **25**, pp. 337-350. DOI: 10.1007/s00382-005-0031-6

Kadioglu, M., Ozturk, N., Erdun, H., and Sen, Z. (1999): On the Precipitation Climatology of Turkey by Harmonic Analysis. *Int. J. Climatol*, **19**, pp. 1717-1728.

Kirtphaiboon, S., Wongwises, P., Limsakul, A., Sooktawee, S., Hamphries, U. (2014): Rainfall Variability over Thailand Related to the EI Nino-Southern Oscillation (ENSO), *Journal of Sustainable Energy & Environment*, **5**, pp. 37-42.

Mantua, N.J., Hare, S.R., Zhang, Y., Wallace, J.M., and Francis, R.C. (1997): A Pacific interdecadal climate oscillation with impacts on salmon production. *Bulletin of the American Meteorological Society*, **78**, pp. 1069-1079.

McSweeney, C.F., Jones, R.G., Lee, R.W., and Rowell, D.P. (2015): Selecting CMIP5 GCMs for downscaling over multiple regions, *Clim Dyn*, **44**, pp. 3237-3260. DOI: 10.1007/s00382-014-2418-8

Mekong River Commission (MRC), (2010): *State of the*

Basin Report 2010, Vientiane, Lao PDR, 232 pp. www.mrcmekong.org

Mekong River Commission (MRC) (2012): *The Impact & Management of Floods & Droughts in the Lower Mekong Basin & the Implications of Possible Climate Change*, Working Paper (2011-2015), 117 pp.

Nguyen-Le, D., Matsumoto, J., and Ngo-Duc, T. (2015): Onset of rainy seasons in the Eastern Indochina Peninsula, Journal of Climate, **28**, pp. 5645-5666. DOI: 10.1175/JCLI-D-14-00373.1

Räsänen, T.A., Lindgren, V., Guillaume, J.H.A., Buckley, B.M., and Kummu, M. (2016): On the Spatial and Temporal Variability of ENSO Precipitation and Drought Teleconnection in Mainland Southeast Asia, *Clim. Past Discuss*., **12**, pp. 1889-1905. DOI: 10.5194/cp-12-1889-2016

Raju, K.S., and Nagesh Kumar, D. (2014): Ranking of global climate models for India using multi-criterion analysis. *Clim Res*, **60**, pp. 103-117.

Raju, K. S., Sonali, P., and Nagesh Kumar, D. (2016): Ranking of CMIP5-based global climate models for India using compromise programming, *Theo Appl Climatol.*, **128-3**, pp. 563–574. DOI: 10.1007/s00704-015-1721-6

Rayner, N.A., Parker, D.E., Horton, E.B., Folland, C.K., Alexander, L.V., Rowell, D.P., Kent, E.C., and Kaplan, A. (2003): Global analyses of sea surface temperature, sea ice, and night marine air temperature since the late nineteenth century, *J. Geophys. Res*., **108 (D14)**, p. 4407. DOI:10.1029/2002JD002670

Saji, N.H., Goswami, B.N., Vinayachandran, P.N., and Yamagata, T. (1999): A dipole mode in the tropical Indian Ocean, *Nature*, **401**, pp. 360-363.

Taylor, K.E. (2001): Summarizing multiple aspects of model performance in a single diagram, J. Geophys. Res., **106**, pp. 7183-7192.

Tsai, C.L., Swadhin, K.B., and Takuji, W. (2015): Indo-China Monsoon Indices, *Sci. Rep. 5*, **8107**, pp. 1-10. DOI: 10.1038/srep08107

Villafuerte II, M. Q., and Matsumoto, J. (2015): Significant Influences of Global Mean Temperature and ENSO on Extreme Rainfall in Southeast Asia, *Journal of Climate*, **28**, pp. 1905-1919. DOI: 10.1175/JCLI-D-14-00531.1

Walker, G.T. (1928): World Weather. Monthly Weather Review, **56**, pp. 167-170.

Wang, B., Clemens, S.C., and Liu, P. (2003): Contrasting the Indian and East Asia Monsoons: Implications on Geologic Timescales, *Marine Geology*, **201**, pp. 5-21. DOI: 10.1016/S0025-3227(03)00196-8.

Wang, B., and LinHo (2002): Rainy seasons of the Asian-Pacific monsoon, J. Climate, **15**, pp. 386-398. DOI: 10.1175/15200469(2002)015<0386:ROSTAP>2.0.CO;2.

Wang, B., and Fan, Z. (1999): Choice of South Asian Summer Monsoon Indices, *BAMS*, **80, No. 4**, pp. 629-638.

Wang, B., Wu, R., and Lau, K.M. (2001): Interannual Variability of the ASIAN Summer Monsoon: Contrasts between the Indian and the Western North Pacific-East ASIAN Monsoon, AMS, *Journal of Climate*, **14**, pp. 4073-4090.

Wilks, D.S. (2011): *Statistical Methods in the Atmospheric Sciences*. San Diego: Academic Press. USA. – 3rd ed., 676 pp.

Yatagai, A., Kamiguchi, K., Arakawa, O., Hamada, A., Yasutomi, N., and Kitoh, A. (2012): APHRODITE: Constructing a Long-term Daily Gridded Precipitation Dataset for Asia based on a Dense Network of Rain Gauges, *Bulletin of American Meteorological Society*, DOI:10.1175/BAMS-D-11-00122.1.

Zhang, Y., Bin Wang, T. L., and Wu, G. (2002): Onset of the summer monsoon over the Indochina Peninsula: climatology and Interannual variations, Journal of Climate, **15**, pp. 3206-3221.

(Received June 13, 2017)